Hysteresis of concrete-filled circular tubular (CFCT) T-joints under axial load

Liu Hongqing [1], Shao Yongbo [*1], Lu Ning [1] and Wang Qingli [2]

[1] *School of Civil Engineering, Yantai University, Qingquan Road 32[#], Laishan District, Yantai, Shandong Province, P.R. China, 264005*
[2] *School of Civil Engineering, Shenyang Jianzhu University, Hunnandong Road 9[#], Shenyang, Liaoning Province, P.R. China, 110168*

Abstract. This paper presents investigations on the hysteretic behavior of concrete-filled circular tubular (CFCT) T-joints subjected to axial cyclic loading at brace end. In the experimental study, four specimens are fabricated and tested. The chord members of the tested specimens are filled with concrete along their full length and the braces are hollow section. Failure modes and load-displacement hysteretic curves of all the specimens obtained from experimental tests are given and discussed. Some indicators, in terms of stiffness deterioration, strength deterioration, ductility and energy dissipation, are analyzed to assess the seismic performance of CFCT joints. Test results indicate that the failures are primarily caused by crack cutting through the chord wall, convex deformation on the chord surface near brace/chord intersection and crushing of the core concrete. Hysteretic curves of all the specimens are plump, and no obvious pinching phenomenon is found. The energy dissipation result shows that the inelastic deformation is the main energy dissipation mechanism. It is also found from experimental results that the CFCT joints show clear and steady stiffness deterioration with the increase of displacement after yielding. However, all the specimens do not perform significant strength deterioration before failure. The effect of joint geometric parameters β and γ of the four specimens on hysteretic performance is also discussed.

Keywords: concrete-filled circular tubular (CFCT) T-joints; hysteretic behavior; experimental study; failure mode; energy dissipation

1. Introduction

The utilization of CFCT structures has been paid much attention in recent decades, and such structures are extensively used in the construction of arch bridges, towers, and high-rise buildings. Some of these structures are exposed to seismic action when they are located in possible earthquake-prone regions. In a CFCT joint, one or several brace tubes are generally connected onto the outer surface of a chord member using penetration weld to form a welded tubular joint. In most cases, the brace of a tubular joint is subjected to axial loading, which causes the chord to sustain loading in radial direction. As it is well known that for a circular chord member with hollow section, its stiffness in radial direction is much smaller than that of the brace in axial

∗Corresponding author, Professor, E-mail: cybshao@ytu.edu.cn

direction. Hence, the chord is very weak in resisting radial load, and local buckling or yielding may occur on the chord surface at the weld toe. Due to this point, filling chord members with concrete is an effective way to restrict the local failure around the brace/chord intersection. However, high stress concentration and residual stress also exist at this location, which is mainly induced by discontinuous stiffness and welding process respectively. The two factors can make the joint perform brittle manner easily, especially under severe seismic action. At present, dynamic and quasi-static tests are primarily used to evaluate earthquake resistance of structures. In this paper, the quasi-static experimental test is then used to study the hysteretic behavior of CFCT T-joints.

In recent years, studies on concrete-filled tubular structures are mainly focused on static and fatigue performance. Hou *et al*. (2013, 2014) conducted experimental and numerical study on concrete-filled circular steel tubes subjected to local lateral loading and established design formulae to calculate the ultimate strength, and some recommendations were also given for practical design. Feng and Young (2008, 2010) carried out tests on square and rectangular stainless steel tubular T-joints and X-joints with concrete-filled in the chord members, and design equations were proposed to predict the loading bearing capacity. Chen *et al*. (2010) performed an experimental study on stress concentration factors of circular hollow section T-joints with concrete filling chords under a combination of axial and in-plane bending loading. The test results indicate that the concrete could significantly reduce the peak stress concentration factors. Mashiri and Zhao (2010) conducted tests on square T-joints subjected to in-plane bending both with concrete-filled chords and with hollow section to investigate their fatigue behavior. The results show that the concrete-filled tubular T-joints exhibit a better fatigue strength in comparison with the empty hollow section ones. Qian *et al*. (2014) studied fatigue performance and residual strength of CFCT X-joints. However, no research has yet been reported on hysteretic behavior of CFCT T-joints subjected to quasi-static cyclic loading.

Previous research work on hysteretic behavior of tubular joints is mainly focused on hollow cross section. Wang and Chen (2007) conducted tests on circular hollow section (CHS) T-joints subjected to cyclic axial and in-plane bending loading to investigate their hysteretic behavior. It is found that such CHS T-joints have different failure modes under various loading conditions. Qin *et al*. (2001) studied the structural performance of completely overlapped joints under static cyclic loading. The test results show that local buckling of the intersection area is the main energy dissipation mechanism. Shao *et al*. (2011a) carried out experimental investigations on CHS T-joints with collar-plate reinforcement as well as corresponding un-reinforced specimens to asses their earthquake resistance. It is obtained from the research work that the reinforced specimens can absorb more energy and undergo larger plastic deformation before failure. Shao *et al*. (2011a) presented experimental and numerical analyses on stiffened and un-stiffened square tubular T-joints under axial cyclic loading. The research results indicate that the stiffened tubular joints exhibit better hysteretic performance compared to the un-stiffened ones. Yin *et al*. (2009) studied experimentally the hysteretic performance of tubular N-joints reinforced with a doubler plate or concrete filling in chord member. It is found that the two stiffened methods can reduce the ductility, but the static capacity is significantly increased. Additionally, some researches on hysteretic behavior of CFCT column-to-beam connections were also conducted (Han and Li 2010, Li and Han 2011, Han *et al*. 2011, Li *et al*. 2013, Sheet *et al*. 2013, Kang *et al*. 2001).

This study then aims to present experimental investigation on the hysteretic behavior of CFCT T-joints subjected to axial cyclic loading at the brace end. The primary objectives of this study include three aspects: (1) to investigate the failure modes and load-displacement hysteretic curves

of CFCT T-joints under cyclic loading ; (2) to conduct research on some indicators, in terms of stiffness deterioration, strength deterioration, ductility and energy dissipation, which are used to assess the seismic performance ; (3) to analyze the effects of various joint geometric parameters such as β and γ values on the hysteretic behavior of CFCT T-joints.

2. Analytical analysis

2.1 Test specimens

Overall four CFCT T-joints are designed for hysteretic tests, and Fig. 1 shows the schematic view of the four tested specimens. Some normalized geometric parameters, which are generally used to describe a tubular T-joint, are also illustrated. To ensure the welding quality, the brace is profiled at end before it is welded onto the outer surface of the chord. The geometric dimensions and the concrete grades of the specimens (named SP-A1, SP-A2, SP-B1 and SP-B2 respectively) are listed in Table 1. D and T are the outer diameter and the wall thickness of the chord respectively. d and t denote the outer diameter and the wall thickness of the brace respectively. L and l are the chord length and the brace length respectively. All the dimensions are expressed in a unit of mm. The tubes of the specimens are fabricated with Q235 carbon steel which is considered as a normal strength material and is commonly used in Chinese constructional structures. Before experimental tests, tensile coupon specimens are fabricated to measure the mechanical properties of the steel materials, and the obtained results are tabulated in Table 2. For the used steel materials, the tensile stresses are higher than the yield stresses since the steel materials have a distinct hardening stage in the tensile process.
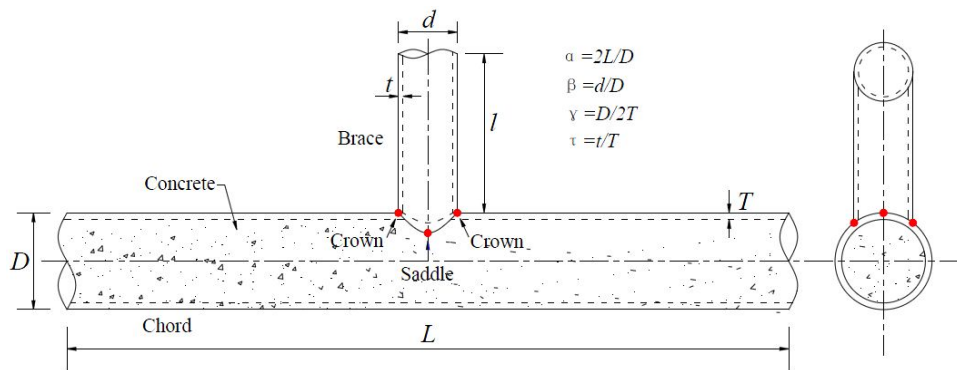

Fig. 1 Schematic view of test specimen

Table 1 Geometric dimensions and concrete grades of T-joint specimens

Specimens	$D \times T$ (mm×mm)	$d \times t$ (mm×mm)	L (mm)	l (mm)	β	γ	α	Concrete grades
SP-A1	219 × 6	102 × 6	1630	360	0.46	18.25	14.89	C40
SP-A2	219 × 6	133 × 6	1630	360	0.61	18.25	14.89	C40
SP-B1	159 × 4.5	76 × 4.5	1680	400	0.48	17.67	21.13	C30
SP-B2	159 × 6	76 × 6	1680	400	0.48	13.25	21.13	C30

Table 2 Properties of steel tubes

Steel tube	Yield strength f_y (MPa)	Ultimate strength f_u (MPa)	Elastic modulus E (GPa)
$\phi76 \times 4.5$	387.92	554.59	199.3
$\phi102 \times 6$	325.16	482.93	185.63
$\phi133 \times 6$	300.6	486.56	209.4
$\phi159 \times 4.5$	366.01	539.66	205.36
$\phi159 \times 6$	353.03	530.45	198.34
$\phi219 \times 6$	288.36	463.79	188.74

Table 3 Mix proportions of concrete (to the weight of cement)

Concrete grades	Cement	Water	Fine aggregate	Coarse aggregate
C40	1	0.42	1.5	2.78
C30	1	0.58	1.91	3.11

The concrete mix filled in the chord members is made of cement, water, coarse aggregate, fine aggregate and some amount of water reducing admixture. The water-cement ratios and proportions of the coarse and fine aggregates are configured to meet the requirements of CIDECT (1995) which specifies that concrete grade lower than C20/25 is not allowed and a grade higher than C50/60 should not be used without further investigation for composite structures. In this study, the concrete grades used to fill the chord tubes are C40 and C30 respectively. C40 concrete is used for specimens SP-A1 and SP-A2, and C30 concrete is used for specimens SP-B1 and SP-B2. The design mix of these two grades of concrete is given in Table 3. The compressive strengths of the concrete are measured from compressive tests on standard concrete cubic specimens with a size of $150 \times 150 \times 150$ mm as shown in Fig. 2, and the corresponding results are 47.6 MPa and 33.3 MPa respectively.

2.2 Test setup

The test setup on conducting the performance of the four CFCT T-joints is shown in Fig. 3. During the experimental process, both ends of the chord are pinned to the supports of the test rig, and axial cyclic load is applied at the brace end. The applied load is produced through an actuator with a maximum loading capacity of ± 500 KN, and the corresponding magnitude of the axial displacement is ± 75 mm. To obtain the load-displacement hysteretic curves of the specimens, the applied cyclic load as well as the displacement at the brace end is recorded automatically by a monitoring system. As shown in Fig. 4, four displacement transducers (named D1, D2, D3 and D4 respectively) are placed at some key points to measure the displacement. The selected points are all located at the outer surface of the chord. D1 and D2 are located at two crown positions, and D3 and D4 are placed on the side wall of the chord. Along the axial direction, D3 is located at the mid-span and D4 is placed at the position just below D2. Additionally, to verify the actual applied load at the brace end, four strain gauges are uniformly placed around the outer surface of the brace at the mid-length of the brace. The displacements and the strains are also recorded by corresponding date acquisition system during the testing process.

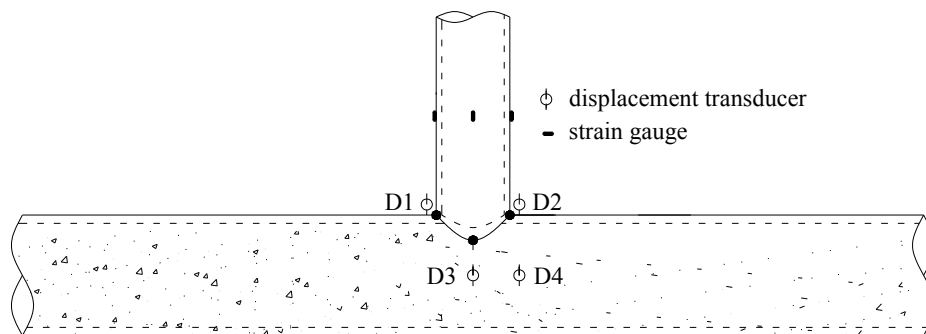Fig. 2 Compressive test on measuring concrete strength

Fig. 3 View of test setup

Fig. 4 Arrangement of measuring instruments

2.3 Loading scheme

The loading scheme in the experimental tests consists of two choices: loading control and displacement control. Loading control is used in the linear stage of the load-displacement relationship. However, it is difficult to control the loading increment after the specimens begin to yield because large deformation may occur at the chord surface with a small loading increment after yielding in the load-displacement curve. Therefore, the vertical displacement at the brace end
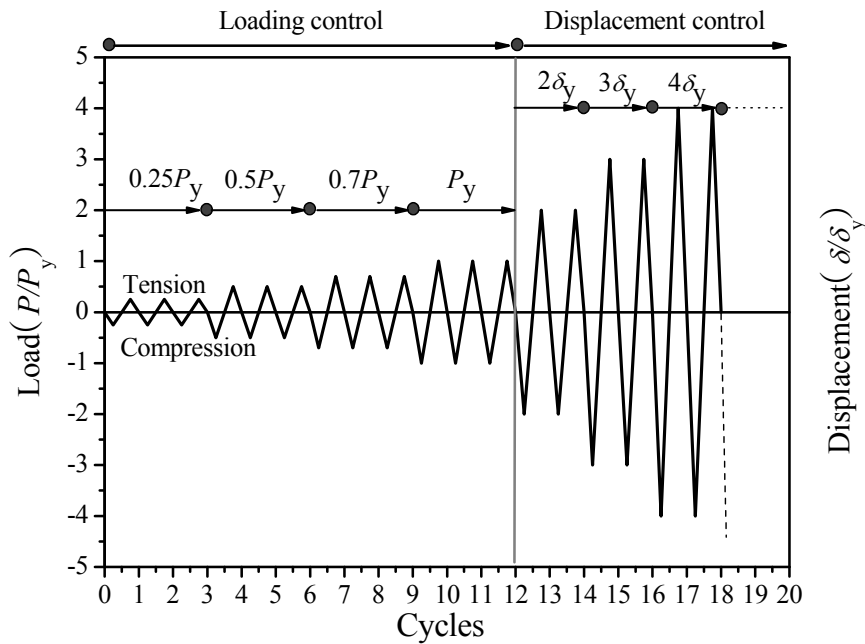
Fig. 5 Loading procedure for T-joint specimens

Table 4 Applied force at loading control stage

Specimens	Yield load P_y (kN)	Applied load (kN)		
		$0.25P_y$	$0.5P_y$	$0.7P_y$
SP-A1	152	38	76	106.4
SP-A2	161	40.3	80.5	112.7
SP-B1	70	17.5	35	49
SP-B2	90	22.5	45	63

is used to control the loading application in this stage. According to the proposal of ATC-24 (1992), the loading procedure is selected as shown in Fig. 5. Three same repeated triangular loading cycles are applied in the following loading amplitudes: $0.25P_y$, $0.5P_y$, $0.7P_y$, and P_y. P_y is the yielding load in the load-displacement curve which is estimated from a finite element simulation on the static behavior of the specimens. Afterward, two same repeated loading cycles are applied in the following displacement amplitudes: $2\delta_y$, $3\delta_y$, $4\delta_y$, $5\delta_y$, etc up to failure of the specimen. δ_y is the displacement corresponding to the yielding load. Both geometric and material nonlinearities are taken into consideration in the finite element analyses for the yielding loads and the corresponding yielding displacements. Considering the maturity in calculating the load carrying capacity of CFCT joints by using finite element analyses, this method is not described in details in this paper. The yielding load P_y for the four specimens calculated from the finite element analyses and the corresponding applied load at brace end in the testing process are listed in Table 4.

3. Experimental result

3.1 Failure modes

In the test for the specimen SP-A1 which has a small value of β compared to specimen SP-A2, clear flexural deformation of the chord is observed both in tension and compression stage after the first cycle with a displacement amplitude of $3\delta_y$ although no crack initiates. In the next loading cycle, it is found that a small crack initiates at the crown position along the weld toe (point A in Fig. 6) in the tensile stage, and the corresponding load at the brace end measured from the instrument is about 246 kN. In the following loading process, the crack propagates along the weld toe gradually. Furthermore, a clear convex deformation occurs on the chord wall near the weld toe around the brace/chord intersection, and such phenomenon is also observed at the chord bottom at the mid-span of the specimen as seen in Fig. 6. This convex deformation is produced due to a large of plastic deformation, and such deformation cannot develop inward to the chord tube because of the restriction of infilled concrete. With the further development of such plastic convex deformation, the crack extends in the chord wall thickness direction and along the circumference of the chord quickly. After the displacement amplitude at the brace end reaches a value of $10\delta_y$, the crack cuts through the chord wall, and nearly 1/5 of the arc length of the chord is cracking. As a deep and long crack significantly degrades the stiffness of the joint, the loading magnitude of the specimen after this cycle begins to drop. In the final cycle with a displacement amplitude of $11\delta_y$, the loading drops suddenly in the tensile stage due to the continuing crack propagation, and the experimental test is completed. The final failure mode of the specimen SP-A1 is shown in Fig. 6.

For specimen SP-A2, a larger value of β compared to specimen SP-A1 is designed. The specimens SP-A1 and SP-A2 have same geometric parameters except a different value of β. At the first loading cycle with a displacement amplitude of $6\delta_y$, a small crack also initiates at the crown position along the weld toe (point A in Fig. 7) in the tensile stage, and the applied load is 292 kN. In comparison with specimen SP-A1, the crack initiates later and the corresponding applied load is larger. In general, when the brace to chord diameter ratio β is big, the crack at the weld toe is difficult to initiate because the stress concentration is lower and it can reduce the brittleness of the material. A big value of β indicates that the brace diameter is large if the diameter of the chord is kept as a constant value. As a result, the contact length, or intersection length, between the chord and the brace surface is longer. Such longer length of the intersection brings a bigger connecting

(a)   (b)
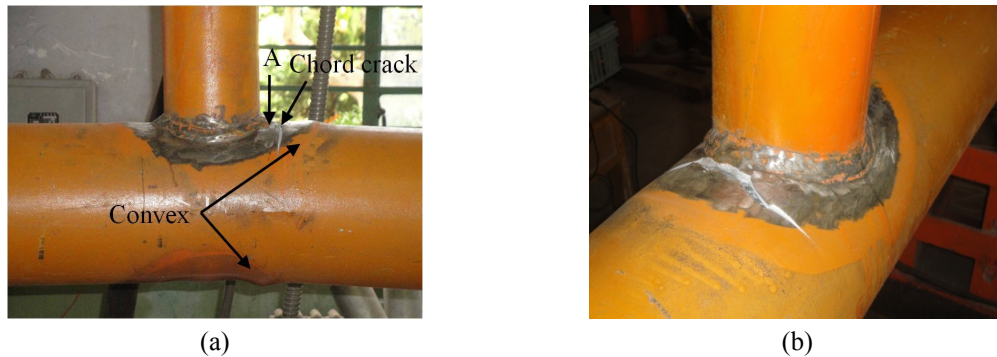
Fig. 6 Typical failure modes of specimen SP-A1

Fig. 7 Typical failure modes of specimen SP-A2

area of the cross section and reduces the stress level. This low stress level is also advantageous for preventing the cracking at the weld toe. With further loading cycles, the crack propagates along the circumferential direction of the chord as well as toward to the chord wall thickness. It is noted that the cracking is not along the weld toe of the brace/chord intersection for both SP-A1 and SP-A2. Quite a clear convex deformation at the mid-span of the chord bottom is also observed during the loading process. However, the convex deformation near the crown position is not a remarkable phenomenon. This is due to the strong resistance of a big brace diameter to local deformation at the joint. Finally, the crack penetrating the chord thickness is developed and the specimen fails. The typical failure of the specimen SP-A2 is illustrated in Fig. 7.

For specimens SP-B1 and SP-B2, they have same dimensions except a different value of chord thickness. The observations for the two specimens during the test process are described briefly as follows: Before the loading cycle with a displacement amplitude of $7\delta_y$, there is no crack initiation at the weld toe. Afterwards, small crack forms at the crown position (point A in Figs. 8 and 9 respectively) and propagates in the tensile stage. With the increase of the applied displacement amplitude at the brace end, the cracks extend and plastic convex deformation initiates both on the chord surface near the crown and on the chord bottom at the mid-span. The failure modes of specimens SP-B1 and SP-B2 are shown in Figs. 8 and 9 respectively.

Fig. 8 Typical failure modes of specimen SP-B1

(a)   (b)

Fig. 9 Typical failure modes of specimen SP-B2

It is found from the experimental test that the crack initiates firstly at the crown position, which is in accordance with the peak hot spot stress position measured by strain gauges in the literature (Chen *et al*. 2010). For the four specimens, plastic convex deformation of the chord wall is also observed during the test process. This phenomenon is much different from T-joints with hollow section. When a circular hollow section (CHS) T-joint is under cyclic loading at brace end, concave deformation also occurs on the chord surface around the brace/chord intersection in the compressive loading stage. The result has been proved by Wang and Chen (2007) and Shao *et al*. (2011a, b). Such deformation difference between a concrete-filled tubular T-joint and a circular hollow section T-joint is mainly caused by the stiffness at the intersection because a concrete-filled chord tube has a much stronger flexural stiffness in its radial direction compared to a hollow section tube with thin wall. When the specimen with concrete filling in the chord member is in compression, the concave deformation on the chord surface near the weld toe is restricted by the infilled concrete. While the specimen is under the tensile condition, the concave deformation at the bottom of chord surface is also restrained by the existing concrete. With the repeated compressive and tensile loading, the convex deformation forms on the chord surface. This is the reason why plastic convex deformation of chord wall is observed in the test process. After the test is completed, the steel tube of a specimen is cut off. The core concrete filling in the chord member is found to be crushed around the intersection as illustrated in Fig. 10. However, the core concrete in other region has no clear crushing failure.
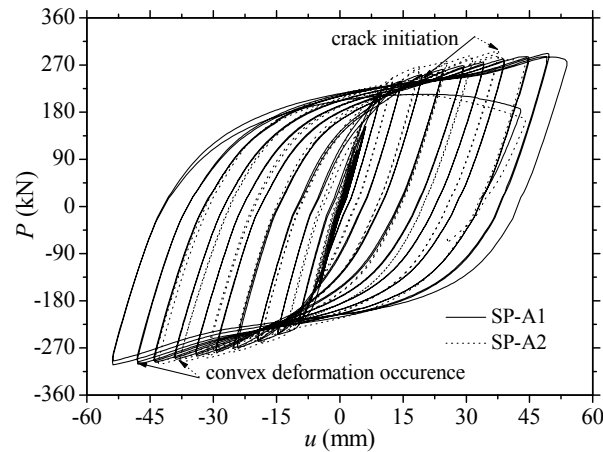

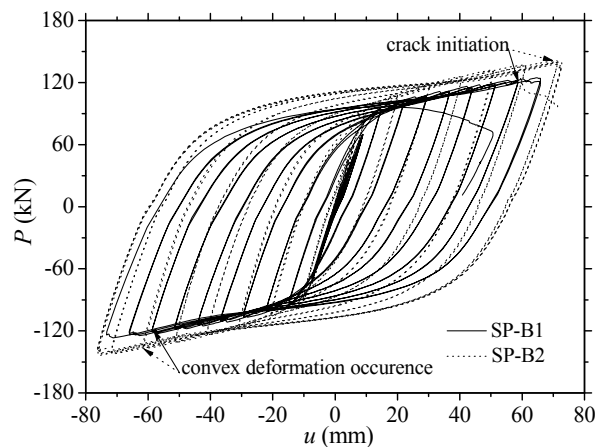Fig. 10 Failure mode of core concrete

3.2 Hysteretic curves

The load-displacement curves of the four specimens obtained from experimental tests are plotted in Figs. 11(a)-(b). The axial displacement u and the corresponding applied axial load P at the brace end are used to plot the hysteretic loops. For comparison purpose, the hysteretic curves of the specimens with different β and γ values are plotted in the same figure. Tensile loading and corresponding displacement are expressed by positive signs, while compressive loading and corresponding displacement are noted by negative signs. In addition, The first crack initiation at the weld and the occurrence of the convex deformation seen from the experimental observation are also marked in these figures.

The hysteretic curves of all the four specimens are much similar in overall shape. Each loop is plump and no obvious pinch phenomenon occurs. The enclosed area of the hysteretic curves is bigger, and it means the specimens absorb much energy before final failure. Although the overall

(a) Specimens SP-A1 and SP-A2

(b) Specimens SP-B1 and SP-B2

Fig. 11 Hysteretic curves of the tested specimen

capacity of energy dissipation seems to be similar, there are still some differences in the hysteretic curves of the four specimens due to their different geometries. For the specimens SP-A1 and SP-A2, the geometric difference is the brace to chord diameter ratio β. SP-A2 has a relatively bigger value of β, which causes a larger intersection area and improves the joint rigidity. Therefore, the applied load magnitude of specimen SP-A2 is higher in each cycle compared to the corresponding loading value of specimen SP-A1 although such difference is not quite big because of a small difference of β value for the two specimens. Another difference is the cracking at the weld for specimen SP-A2 is relatively later compared to specimen SP-A1 because it is obviously observed from hysteretic curves that the cracking of specimen SP-A1 occurs at the displacement amplitude of $3\delta_y$, while cracking of SP-A2 forms at the displacement amplitude of $6\delta_y$. For specimens SP-B1 and SP-B2, the geometric difference is the chord diameter to thickness ratio γ. SP-B2 has a lower value of γ, which implies that its chord thickness is bigger. Clearly, a big wall thickness of a hollow section tube can improve its flexural rigidity greatly, and thus increase its resistance to lateral loading. Although a big wall thickness of the chord may reduce the diameter of the concrete cylinder inside the chord and thus decrease the flexural stiffness of the core concrete, the overall concrete filled tube still has an improved flexural stiffness because the elastic modulus of steel material is much bigger than that of concrete. Additionally, the plasticity and ductility of steel material are also much better than concrete material, and this will improve the energy dissipating capacity of the structure subjected to dynamic loading. This conclusion is found from the tested hysteretic curves in Fig. 11(b) which shows a clear larger curve loop in each loading cycle for specimen SP-B2 compared to SP-B1.
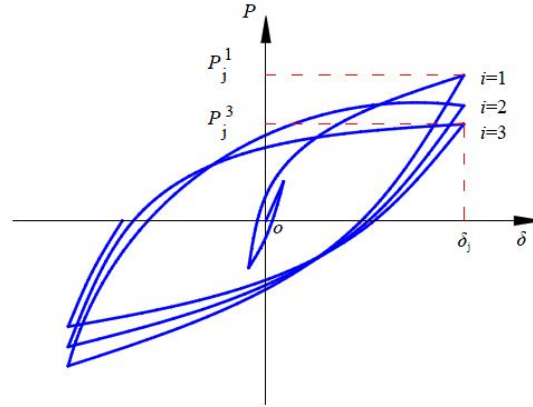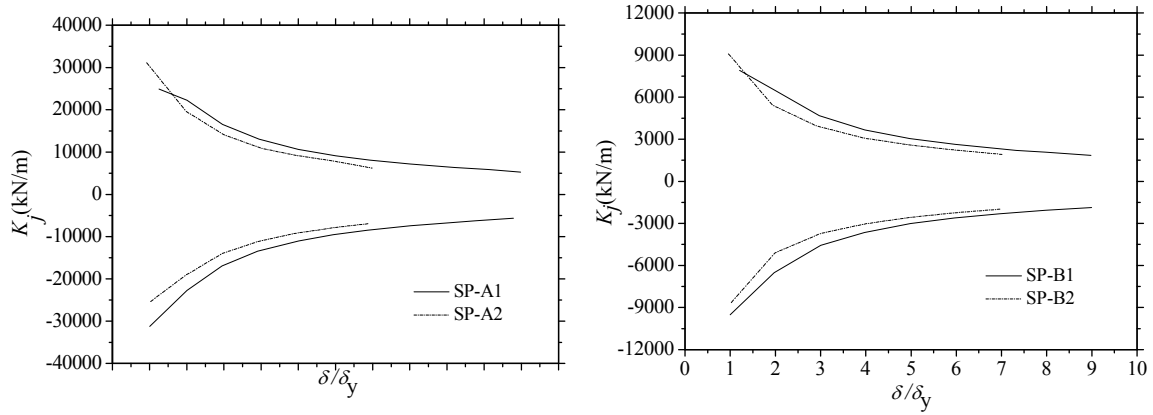
3.3 Stiffness deterioration

From the hysteretic curves in Fig. 11, a stiffness deterioration can be found from the reduced slopes in the linear and nonlinear stages of each loop. To evaluate a stiffness deterioration, an index called looped stiffness coefficient K_j in the literature (JGJ101-96 2010, Liao *et al.* 2014) is defined and it is also used in this study. As shown in Fig. 12, K_j is calculated from the following equation

$$K_j = \frac{\sum_{i=1}^{k} P_j^i}{\sum_{i=1}^{k} u_j^i} \qquad (1)$$

where P_j^i and u_j^i are the peak load and the corresponding displacement respectively under the ith loading cycle when the value of the relative displacement δ / δ_y equals to j, and k is the number of loading cycles. The looped stiffness coefficient K_j specified as an index to describe the stiffness deterioration is mainly determined by two factors, i.e., stiffness deterioration due to the increasing displacement and the repeating cycles at the same displacement level.

The stiffness deteriorations both in tension and compression are plotted in Figs. 13(a)-(b) respectively. The horizontal axis denotes the relative displacement δ / δ_y, and the vertical axis denotes the looped stiffness coefficient K_j. The results indicate that all the specimens show obvious and stable stiffness deterioration as the relative displacement δ / δ_y increases. This is due to the yielding of the steel tube as well as the crushing of the concrete filling in the chord member under cyclic axial loading. It is also found that the relationships of $K_j - \delta / \delta_y$ for the specimens SP-A1 and SP-A2 with different β values are almost identical. Similar phenomenon of the stiffness

Fig. 12 Determination of stiffness deterioration coefficient (K_j)

(a) Specimens SP-A1 and SP-A2   (b) Specimens SP-B1 and SP-B2

Fig. 13 Stiffness deterioration of the specimens

deterioration is also found for the specimens SP-B1 and SP-B2 with different γ values.

3.4 Strength deterioration

Another index namely strength deterioration coefficient λ_i is generally used to assess the strength deterioration in the literature (BS EN 1993-1-1:200 2005, Han and Song 2012). λ_i is defined as a ratio of the ultimate load in each loading cycle to the ultimate load in the first loading cycle at the same displacement level δ / δ_y, and it is calculated as follow

$$\lambda_i = \frac{P_j^i}{P_j^1} \tag{2}$$

where P_j^i is the ultimate load in the ith loading cycle and P_j^1 is the peak load in the first loading cycle when the relative displacement δ / δ_y equals to j. The typical $\lambda_i - \delta / \delta_y$ curves of the four

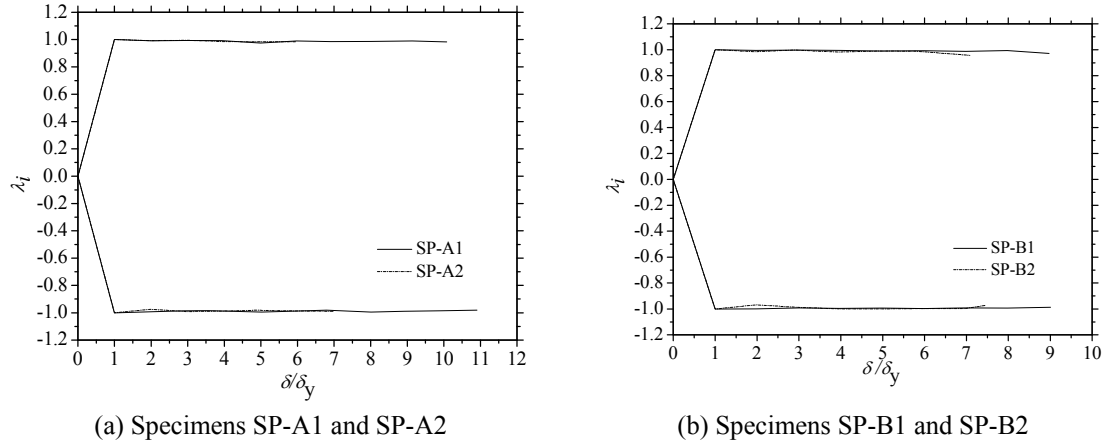(a) Specimens SP-A1 and SP-A2   (b) Specimens SP-B1 and SP-B2

Fig. 14 Strength deterioration of the specimens

specimens are presented in Figs. 14(a)-(b). The results show that the specimens do not show significant strength deterioration at the same displacement level of δ / δ_y.

To study the strength deterioration of a CFCT joint in the entire loading process, an index called overall strength deterioration factor λ_j is defined in the literature (Han and Song 2012), and it is calculated from the following equation

$$\lambda_j = \frac{P_j}{P_{max}} \tag{3}$$

where P_j is the peak load obtained from hysteretic curves at the displacement level of δ / δ_y, and P_{max} is the maximum peak point in the whole loading process. i.e., P_{max} is the ultimate load carrying capacity of the specimens. The $\lambda_j - \delta / \delta_y$ curves of the four specimens are given in Figs. 15(a)-(b). It is easily found that the specimens can all sustain large plastic deformation after
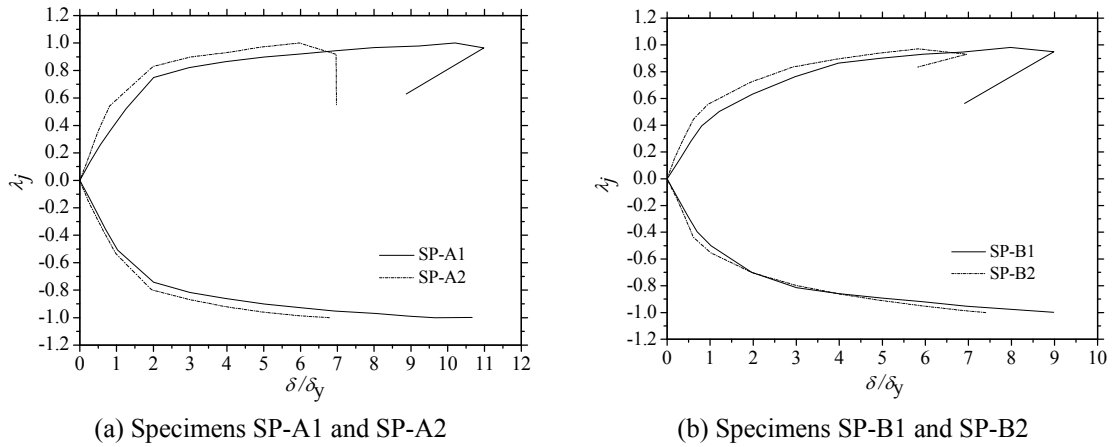

(a) Specimens SP-A1 and SP-A2   (b) Specimens SP-B1 and SP-B2

Fig. 15 Overall strength deterioration of the specimens

(a) Specimens SP-A1 and SP-A2   (b) Specimens SP-B1 and SP-B2
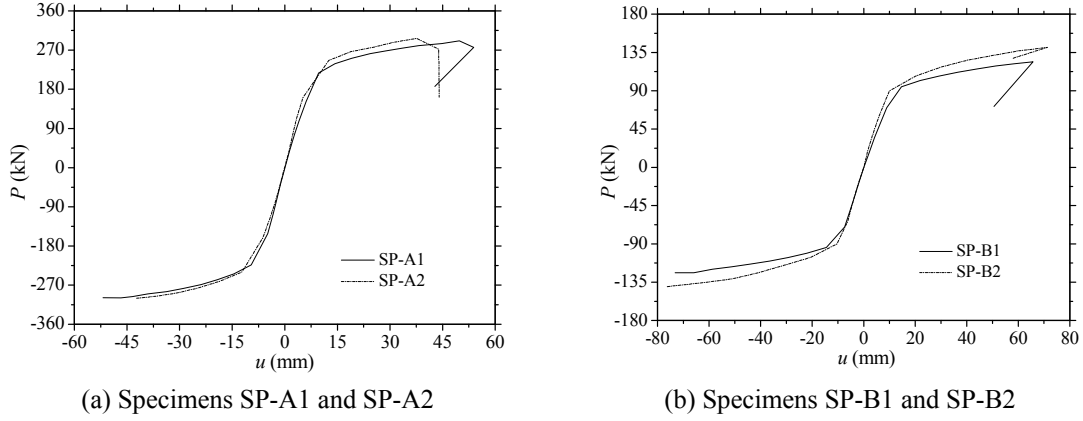
Fig. 16 Skeleton curves of the four tested specimens

yielding before final failure. SP-A2 has a higher value of λ_j compared to SP-A1, which means its strength deterioration is lower. For specimen SP-B2, it also has a higher value of λ_j compared to SP-B1.

3.5 skeleton curve and ductility ratio

It has been experimentally proved that it is reasonable to use the skeleton curves of cyclic performance to estimate the monotonic response of a structure or a component. Therefore, the ultimate load of a CFCT T-joint can be measured approximately by the peak load on the skeleton curve. Skeleton curves for the four specimens obtained by connecting the peak points in every loading cycle of the hysteretic curves are shown in Figs. 16(a)-(b). For comparison purpose, the skeleton curves of the specimens with different β or γ values are plotted in the same figure. As the four specimens all fail in the tensile stage, the tensile maximum load obtained from the skeleton curves can be taken as the ultimate load bearing capacity. The maximum load carrying capacity of specimens SP-A1, SP-A2, SP-B1 and SP-B2 are 291 kN, 297 kN, 124 kN and 141 kN respectively. Similar conclusions can be drawn from the skeleton curves: Compared to SP-A1, SP-A2 can sustain a bigger load before failure but it experiences a smaller deformation at failure. For SP-B2, it can both sustain a bigger load before failure and experience a larger deformation at failure in comparison with SP-A1. However, as can been seen from Fig. 15(b), the relative displacement δ / δ_y of SP-B2 is smaller than that of SP-B1 due to a bigger yielding displacement of δ_y, and this means that SP-B2 undergoes a larger elastic deformation compared to SP-B1 in the test process.

In additional to the ultimate load carrying capacity of CFCT joints, ductility plays an important role in earthquake resistance design. The ductility can reflect the capacity of the inelastic deformation for a structure without significant decrease in the load carrying capacity before failure. Generally, the ductility is assessed by calculating the ductility ratio, which is defined as follows

$$\mu^+ = \delta_u^{\ +}/\delta_y^{\ +} \quad \text{at tensile stage} \tag{4}$$

$$\mu^- = \delta_u^{\ -}/\delta_y^{\ -} \quad \text{at comprssive stage} \tag{5}$$

Table 5 Ductility ratio of the T-joint specimens

Specimens	δ_y^+(mm)	δ_u^+ (mm)	δ_y^- (mm)	δ_u^- (mm)	$\mu^+ = \delta_u^+ / \delta_y^+$	$\mu^- = \delta_u^- / \delta_y^-$
SP-A1	6.1	53.9	-4.9	-53.9	8.8	11.0
SP-A2	5.2	43.9	-6.3	-43.9	8.4	6.9
SP-B1	8.8	65.7	7.3	73.2	7.4	10.0
SP-B2	9.9	71.3	10.2	75.8	7.2	7.4

where δ_u^+ and δ_u^- are the displacements corresponding to the ultimate load in the tension stage and in the compression stage respectively, and δ_y^+ and δ_y^- are the yielding displacements in the tension and in the compression half cycles respectively. μ^+ and μ^- are the ductility ratios in the tensile and in the compressive stages respectively.

For a structure, it can undergo a larger plastic deformation under seismic performance when the value of the ductility ratio is bigger. The ductility ratios of the four CFCT T-joint are presented in Table 5. It can be seen from Table 5 that all the specimens have large ductility ratios both in tensile and in compressive stages. However, the ductility ratios of specimen SP-A1 are larger compared to specimen SP-A2, and SP-B1 has a larger value of ductility ratio compared to SP-B2.

3.6 Energy dissipation

The energy dissipation capacity of a CFCT joint is also a critical factor to estimate its seismic resistance when this joint is subjected to earthquake action. The dissipated energy can be obtained by calculating the area enveloped by the load-displacement curves. A coefficient termed as accumulative energy dissipation ratio η_a is used to measure the energy dissipation. At present, different methods have been proposed by researchers to calculate the energy dissipation ratio η_a. In this paper, two methods are adopted to measure the ratio η_a of a CFCT T-joint. Based on the definition in Ref. (Wang and Chen 2007), the ratio η_a is defined as follow

$$\eta_a = \sum_{i=1}^{n}(E_i^+ + E_i^-)/E_y \tag{6}$$

Where E_i^+ and E_i^- are the dissipated energy in the tensile and in the compressive stages of each loading cycle respectively. E_y is the absorbed energy at the first yield displacement δ_y, and n is the total number of the loading cycles in the test process. E_y can be calculated from the following equation

$$E_y = P_y \delta_y / 2 \tag{7}$$

where P_y is the load corresponding to the first yielding point in the hysteretic curves.

The absorbed energy value of the CFCT joints may vary at the first tensile and compressive yielding points in the hysteretic curves owning to different hysteretic behavior in the tensile and in the compressive phases. The energy dissipation at the first tensile and in the first compressive yielding points are defined as E_y^+ and E_y^- respectively. For a safety purpose, E_y is taken as a larger value between the E_y^+ and E_y^-. According to the definition in Ref. (Shao *et al*. 2011a, b), the ration η_a is specified as follow

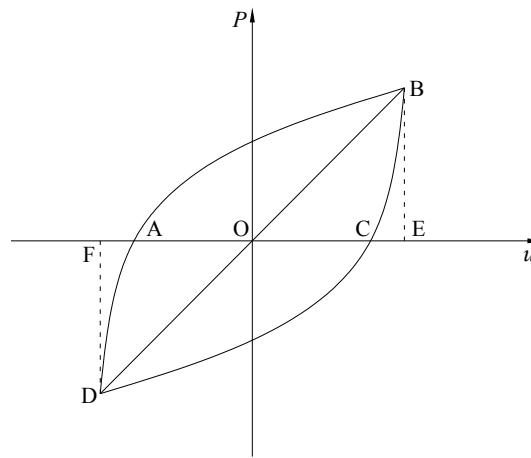$$\eta_a = (S_{ABC} + S_{CDA})/(S_{OBE} + S_{ODF}) \tag{8}$$

Fig. 17 Definition of envelop curve

This definition can be explained in Fig. 17. S_{ABC} and S_{CDA} are the areas enclosed by the curve ABC in the tensile stage and by the curve CDA in the compressive stage respectively. S_{OBE} and S_{ODF} are the enclosed area of the triangle OBE and ODF respectively.

The energy dissipation details of the four specimens calculated by the above two methods are both tabulated in Tables 6-7 respectively. It can be seen from Tables 6-7 that the different two methods draw similar conclusion. The energy dissipation ratios are quite big for all the specimens, and it indicates that all the specimens undergo accumulative inelastic deformation before final failure, and such inelastic deformation is the main energy dissipation mechanism for the CFCT joints. For specimen SP-A1, its energy dissipation ratio is bigger than SP-A2, and this implies that more plastic energy dissipated for SP-A1 compared to SP-A2.

Table 6 Accumulate energy dissipation ratio of the tubular T-joints (Wang et al, 2007)

Specimens	$\sum_{i=1}^{n}(E_i + E_i^-)$	E_y (kN·m)	E_y^- (kN·m)	E_y (kN·m)	η_a
SP-A1	325.99	0.46	0.37	0.46	708.67
SP-A2	158.65	0.42	0.5	0.5	317.3
SP-B1	158.88	0.31	0.26	0.31	512.5
SP-B2	240.86	0.45	0.47	0.47	512.47

Table 7 Accumulate energy dissipation ratio of the tubular T-joints (Shao et al, 2011)

Specimens	$S_{ABC+CDA}$ (kN·m)	$S_{OBE+ODF}$ (kN·m)	η_a
SP-A1	35.86	0.83	43.2
SP-A2	28.08	0.92	30.52
SP-B1	18.99	0.57	33.31
SP-B2	30.22	0.92	32.85

4. Conclusions

Experimental study on CFCT T-joints under quasi-static cyclic axial loading has been carried out to investigate their hysteretic performance. The failure modes, the hysteretic curves, the stiffness and the strength deterioration, the energy dissipation and the ductility are all analyzed in details. Based on experimental results and analyses, the following conclusions can be obtained.

- The failure modes of CFCT T-joints are mainly induced by cracking and convex plastic deformation of the chord wall as well as the crushing of the core concrete. Due to the improved joint rigidity by the concrete, local deformation on the chord surface around the brace/chord intersection is prevented greatly.
- The hysteretic curves of the four specimens show a plump without obvious pinching phenomenon. From the hysteretic curves, the ductility ratio and the energy dissipation ratios are calculated. The results show that the CFCT T-joints all have good energy dissipating capacity, and the inelastic deformation is the main energy dissipation mechanism.
- For CFCT T-joints under quasi-static cyclic loading, they have stable stiffness deterioration as the increase of the relative displacement δ / δ_y. This may be caused by the yielding of the steel tube and the crushing of the core concrete as well as material degradation at repeated loading cycles in the test process. However, the strength deterioration is not quite severe until failure.

References

ATC-24 (1992), Guidelines for cyclic seismic testing of components of steel structures, Applied Technology Council; Redwood City, CA, USA.

Bergmann, R., Matsui, C., Meinsma, C. and Dutta, D. (1955), "Design guide for concrete filled hollow section columns under static and seismic loading", Comite International pour le Developpement et 1 Etude de la Construction Tubulaire (CIDECT); Verlag TUV Rheinland, Cologne, Germany.

BS EN 1993-1-1:200 (2005), Eurocode 3: Design of steel structures, Part 1-1: General rules and rules for buildings, European Committee for Standardization.

Chen, J., Chen, J. and Jin, W.L. (2010), "Experimental investigation of stress concentration factor of concrete-filled tubular T joints", *J. Constr. Steel Res.*, **66**(12), 1510-1515.

Feng, R. and Young, B. (2008), "Tests of concrete-filled stainless steel tubular T-joints", *J. Constr. Steel Res.*, **64**(1), 1283-1293.

Feng, R. and Young, B. (2010), "Design of concrete-filled stainless steel tubular connections", *Adv. Struct. Eng.*, **13**(3), 471-492.

Han, L.H. and Li, W. (2010), "Seismic performance of CFST column to steel beam joint with RC slab: Experiments", *J. Constr. Steel Res.*, **66**(1), 1374-1386.

Han, L.H. and Song, T.Y. (2012), *Fire Safety Design Theory of Steel-Concrete Composite Structures*, China Science Press, Beijing, China. [In Chinese]

Han, L.H., Wang, W.D. and Tao, Z. (2011), "Performance of circular CFST column to steel beam frames under lateral cyclic loading", *J. Constr. Steel Res.*, **67**(5), 876-890.

Hou, C., Han, L.H. and Zhao, X.L. (2013), "Concrete-filled circular steel tubes subjected to local bearing force: Experiments", *J. Constr. Steel Res.*, **83**(4), 90-104.

Hou, C., Han, L.H. and Zhao, X.L. (2014), "Concrete-filled circular steel tubes subjected to local bearing force: Finite element analysis", *Thin-Wall. Struct.*, **77**(4), 109-119.

JGJ101-96 (2010), Specification for test methods of seismic building, Architecture Industrial Press of China, Beijing, China. [In Chinese]

Kang, C.H., Shin, K.J., Oh, Y.S. and Moon, T.S. (2001), "Hysteretic behavior of CFT column to H-beam connections with external T-stiffeners and penetrated elements", *J. Eng. Struct.*, **23**(9), 1194-1201.

Li, W. and Han, L.H. (2011), "Seismic performance of CFST column to steel beam joints with RC slab: Analysis", *J. Constr. Steel Res.*, **67**(1), 127-139.

Li, W., Han, L.H. and Ren, Q.X. (2013), "Inclined concrete-filled SHS steel column to steel beam joints under monotonic and cyclic loading: Experiment", *Thin-Wall. Struct.*, **62**(1), 118-130.

Liao, F.Y., Han, L.H. and Tao, Z. (2014), "Behaviour of composite joints with concrete encased CFST columns under cyclic loading: Experiments", *J. Eng. Struct.*, **59**(2), 745-764.

Mashiri, F.R. and Zhao, X.L. (2010), "Square hollow section (SHS) T-joints with concrete-filled chords subjected to in-plane fatigue loading in the brace", *Thin-Wall. Struct.*, **48**(2), 150-158.

Qian, X.D., Jitpairod, K., Marshall, P., Swaddiwudhipong, S., Qu, Z.Y., Zhang, Y. and Pradana, M.R. (2014), "Fatigue and residual strength of concrete-filled tubular X-joints with full capacity welds", *J. Constr. Steel Res.*, **100**(9), 21-35.

Qin, F., Fung, T.C. and Soh, C.K. (2001), "Hysteretic behavior of completely overlap tubular joints", *J. Constr. Steel Res.*, **57**(7), 811-829.

Shao, Y.B., Li, T., Lie, S.T. and Chiew, S.P. (2011a), "Hysteretic behavior of square tubular T-joints with chord reinforcement under axial cyclic loading", *J. Constr. Steel Res.*, **67**(1), 140-149.

Shao, Y.B., Lie, S.T., Chiew, S.P. and Cai, Y.Q. (2011b), "Hysteretic performance of circular hollow section tubular joints with collar-plate reinforcement", *J. Constr. Steel Res.*, **67**(2), 1936-1947.

Sheet, I.S., Gunasekaran, U. and MacRae, G. (2013), "Experimental investigation of CFT column to steel beam connections under cyclic loading", *J. Constr. Steel Res.*, **86**(7), 167-182.

Wang, W. and Chen, Y.Y. (2007), "Hysteretic behavior of tubular joints under cyclic loading", *J. Constr. Steel Res.*, **63**(10), 1384-1395.

Yin, Y., Han, Q.H., Bai, L.J., Yang, H.D. and Wang, S.P. (2009), "Experimental study on hysteretic behavior of tubular N-joints", *J. Constr. Steel Res.*, **65**(2), 326-334.

BU